The 8th European Congress on Computational Methods in Applied Sciences and Engineering
ECCOMAS Congress 2022
5-–9 June 2022, Oslo, Norway

DEVELOPING AN IMMERSED BOUNDARY METHOD FOR COMPRESSIBLE FLOW

FREDERIK KRISTOFFERSEN[1], MARTIN LARSSON[2], SVERRE GULLIKSTAD JOHNSEN[3], WOLFGANG SCHRÖDER[4] AND BERNHARD MÜLLER[1]

[1] Dept. of Energy and Process Engineering
Norwegian University of Science and Technology
Trondheim, Norway

[2] Sportradar AS
Trondheim, Norway

[3] SINTEF Industry
Trondheim, Norway

[4] Institute of Aerodynamics
Rheinisch-Westfälische Technische Hochschule
Aachen, Germany

Key words: Computational Fluid Mechanics, Immersed Boundary Method, Compressible Flow

Abstract. A 3D fluid-structure interaction (FSI) code is under development. The fluid domain (Navier-Stokes) solver will employ a sharp interface ghost node immersed boundary method (IBM) to apply the boundary conditions at fluid-solid interfaces. The Navier-Stokes (N-S) solver has been verified using a classic Poiseuille channel flow. The current version of the immersed boundary method is being tested by solving a heat conduction problem. The order of accuracy of the IBM was shown to be just above second order.

1 INTRODUCTION

Obstructive sleep apnea (OSA) is a sleep related breathing disorder which involves collapses of the pharyngeal airways that can partially or fully obstruct breathing during sleep [1]. For many OSA patients the treatment involves surgery, of which the outcome has proven hard to predict. Computational fluid mechanics (CFD) has been proposed [2, 3] as a tool to aid in predicting whether an OSA patient will benefit from surgery. The human respiratory flow is generally bounded by deformable soft tissue. Thus, this flow problem should be solved as a fluid-structure interaction (FSI) [4, 5, 6].

FSI solvers are often categorized as monolithic or partitioned. A partitioned approach utilizes separate solvers for the domains. These need to communicate throughout the simulation. An advantage of the partitioned approach is that we can use established solvers and numerical methods.

We can also distinguish between FSI solvers that employ body-fitted grids and those with non-conforming grids. Non-conforming grid methods do not require re-meshing, which is a costly process in terms of CPU time. Furthermore, the grid can be structured and Cartesian. However, these methods need more sophisticated methods to apply BCs at boundaries that do not coincide with the grid points or faces. Examples of non-conforming grid methods are cut-cell methods and immersed boundary methods (IBM) [7, 8].

The first IBMs developed [9] have later been categorized as diffuse interface IBMs. Another more recent approach is the sharp interface model [10, 11]. With this model, grid nodes that lie in the solid domain, but close enough to the interface to be included by numerical stencils in the fluid solver, are marked as ghost nodes.

This paper will focus on the fluid solver of a 3D FSI code that is currently under development, and utilizes a ghost point IBM. First, the governing equations are outlined, including the non-dimensionalizing and perturbation form. In Section 3, we give the spatial and temporal discretizations. Additionally, the treatment of immersed boundary conditions will be explained in Section 3.3. Next, two test cases will be introduced, namely 1) channel flow, which is one of the cases that were used to verify the N-S solver, and 2) a heat conduction problem that gives verification for the IBM without the complexity of fluid flow. The verification results are presented and discussed in Section 5.

2 NAVIER-STOKES EQUATIONS FOR COMPRESSIBLE FLOW

The fluid domain of the FSI framework is governed by the Navier-Stokes equations for compressible flow:

$$\frac{\partial}{\partial t}\begin{bmatrix}\rho\\ \rho\mathbf{u}\\ \rho E\end{bmatrix} + \nabla\cdot\left(\begin{bmatrix}\rho\mathbf{u}\\ \rho\mathbf{u}\otimes\mathbf{u}\\ \rho H\mathbf{u}\end{bmatrix} + p\begin{bmatrix}0\\ \mathbf{I}\\ 0\end{bmatrix}\right) = \nabla\cdot\begin{bmatrix}0\\ \boldsymbol{\tau}\\ \boldsymbol{\tau}\mathbf{u}+\kappa\nabla T\end{bmatrix} \quad , \tag{1}$$

where t is time, ρ is the mass density, $\vec{u}$ is the velocity, $H = E + \frac{p}{\rho}$ is the total enthalpy, E is the specific total energy, p is pressure, $\mathbf{I}$ is the identity matrix, ∇ is the nabla operator, κ is the thermal conductivity, T is temperature and

$$\tau_{ij} = \mu\left[\frac{\partial u_i}{\partial x_j} + \frac{\partial u_j}{\partial x_i} - \frac{2}{3}\delta_{ij}\frac{\partial u_k}{\partial x_k}\right] \tag{2}$$

are the components of the viscous stress tensor τ for a Newtonian fluid. Here, μ is the dynamic viscosity and δ_{ij} is the Kronecker delta.

The equations of state for perfect gas yield:

$$p = (\gamma-1)\left(\rho E - \frac{\rho}{2}\left|\vec{u}\right|^2\right) \quad , \tag{3}$$

where γ is the ratio of specific heats.

The transport properties μ and κ are modeled as functions of the temperature T only. The viscosity is given by Sutherland's law:

$$\frac{\mu}{\mu_0} = \left(\frac{T}{T_0}\right)^{1.5}\frac{1+S}{\frac{T}{T_0}+S} \quad , \tag{4}$$

where S is the Sutherland's constant and μ_0 and T_0 are reference states for μ and T, respectively. Assuming constant Prandtl number Pr, the thermal conductivity is given by

$$\kappa = \frac{c_p}{Pr}\mu \quad . \tag{5}$$

where c_p is the specific heat capacity at constant pressure.

The compressible flow approach gives the possibility of investigating acoustic and thermal effects.

The governing equations are non-dimensionalized as follows, where superscript * denotes non-dimensional values and subscript $_0$ denotes reference state:

$$\begin{array}{cccccccc} t^* = \frac{tc_0}{L} & , & x^* = \frac{x}{L} & , & y^* = \frac{y}{L} & , & z^* = \frac{z}{L} \\ \rho^* = \frac{\rho}{\rho_0} & , & u^* = \frac{u}{c_0} & , & v^* = \frac{v}{c_0} & , & w^* = \frac{w}{c_0} \\ T^* = \frac{T}{T_0} & , & p^* = \frac{p}{\rho_0 c_0^2} & , & E^* = \frac{E}{c_0^2} & , & (\rho E)^* = \frac{\rho E}{\rho_0 c_0^2} \\ \mu^* = \frac{1}{Re_0}\frac{\mu}{\mu_0} & , & \kappa^* = \frac{1}{(\gamma-1)Pr_0 Re_0}\frac{\kappa}{\kappa_0} & , & & & & \end{array} \tag{6}$$

where x, y and z are the spatial coordinates, u, v and w are the velocity components in the x, y and z directions respectively. L is a length scale, $Re_0 = \rho_0 c_0 L/\mu_0$ and c_0 are the Reynolds number and speed of sound of the reference state. Choosing these formulations, the non-dimensionalized governing equations will get the same form as the dimensional ones. Thus, the super-index * is dropped from here on.

The Mach number is defined as $Ma = |\mathbf{u}|/c_0$. To minimize cancellation errors for low Mach number flow, the perturbation formulation [12] is adopted. This means that we use the flow variables' perturbations around a reference state instead of the variables themselves. We decompose the flow variables as

$$\phi = \phi_0 + \phi' \quad , \tag{7}$$

where ϕ is any flow variable, ϕ_0 denotes reference state and ϕ' is the perturbation. This is done for conserved variables and primitive variables, but not transport properties. Setting the reference state of the velocity to zero, the governing equations retain their forms, except for the convective flux in the energy equations, which is changed from $\rho H \vec{u}$ to $((\rho H)_0 + (\rho H)')\,\vec{u'}$.

3 NUMERICAL MODEL

3.1 Discretization in Space

The spatial discretization of the fluid domain is done by second order central difference operators. Thus, first derivatives, e.g. in the continuity equation are approximated as

$$\frac{\partial(\rho u)}{\partial x} \approx \frac{(\rho u)_{i+1} - (\rho u)_{i-1}}{2\Delta x} \quad . \tag{8}$$

Mixed derivatives, as found in the viscous terms of the Navier-Stokes equation, are discretized by applying the second order operator twice,

$$\frac{\partial}{\partial y}\left[\mu\frac{\partial u}{\partial x}\right] \approx \frac{1}{4\Delta x \Delta y}\left[\mu_{i,j+1}(u_{i+1,j+1} - u_{i-1,j+1}) - \mu_{i,j-1}(u_{i+1,j-1} - u_{i-1,j-1})\right] \quad . \tag{9}$$

In the case of repeated derivatives, applying the operator twice would result in a wider stencil. Instead, the compact second derivative scheme is used, where the viscosity at the adjacent midpoints are computed as averages,

$$\frac{\partial}{\partial x}\left[\mu\frac{\partial u}{\partial x}\right] \approx \frac{1}{2\Delta x^2}\left[(\mu_{i+1}+\mu_i)(u_{i+1}-u_i)-(\mu_i+\mu_{i-1})(u_i-u_{i-1})\right] \quad . \tag{10}$$

The compact stencil Eq.(10) is also used for the thermal diffusion terms in the energy equation and the heat equation. Besides being compact this discretization has the added benefit of better damping of high wave number oscillations.

3.2 Discretization in Time

The spatial discretization of the Navier-Stokes equations for compressible flow Eq.(1) and of the heat equation Eq.(25) in the interior of the domain leads to the system of ordinary differential equations

$$\frac{d\phi^n_{ijk}}{dt} = R(\{\phi_{ijk}\}^n, t) \quad . \tag{11}$$

The temporal discretization is done using the fourth order explicit classical Runge-Kutta method (RK4).

$$\phi^{n+1}_{ijk} = \phi^n_{ijk} + \frac{\Delta t^n}{6}\left(k^n_{1,ijk} + 2k^n_{2,ijk} + 2k^n_{3,ijk} + k^n_{4,ijk}\right) \quad , \tag{12}$$

where

$$k^n_{1,ijk} = R(\{\phi_{ijk}\}^n, t^n) \quad , \tag{13}$$

$$k^n_{2,ijk} = R(\{\phi_{ijk} + \Delta t^n \frac{k_{1,ijk}}{2}\}^n, t^n + \frac{\Delta t^n}{2}) \quad , \tag{14}$$

$$k^n_{3,ijk} = R(\{\phi_{ijk} + \Delta t^n \frac{k_{2,ijk}}{2}\}^n, t^n + \frac{\Delta t^n}{2}) \quad , \tag{15}$$

$$k^n_{4,ijk} = R(\{\phi_{ijk} + \Delta t^n \cdot k_{3,ijk}\}^n, t^n + \Delta t^n) \quad . \tag{16}$$

The time-step size Δt is chosen as large as possible, without exceeding the stability criteria for the heat conduction and channel flow cases (cf. Section 4), respectively:

$$\Delta t_{heat\ eq.} \leq \frac{\Delta x^2}{6\alpha} \quad , \quad \Delta t_{N-S} \leq min\{\Delta t_{CFL}, \Delta t_{visc}\} \quad , \tag{17}$$

$$\Delta t_{CFL} = C_{CFL}\left(\frac{|u|+c}{\Delta x} + \frac{|v|+c}{\Delta y} + \frac{|w|+c}{\Delta z}\right)^{-1} \quad , \tag{18}$$

$$\Delta t_{visc} = \frac{C_{RK4}}{\frac{\mu}{\rho} max\{\frac{4}{3}, \frac{\gamma}{Pr}\}}\left(\frac{1}{\Delta x^2} + \frac{1}{\Delta y^2} + \frac{1}{\Delta z^2}\right)^{-1} \quad , \tag{19}$$

where α is thermal diffusivity and C_{CFL} and C_{RK4} are constants.

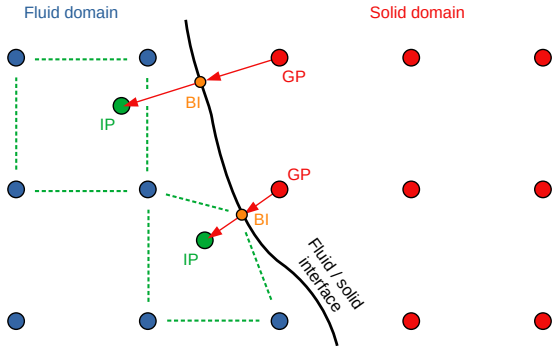

Figure 1: Sketch of ghost points (GP), body intercept (BI) points and image points (IP).

3.3 Boundary Conditions at Immersed Boundaries

Figure 1 shows how we classify the nodes and points close to an immersed boundary. The term *ghost node* here refers to a node that is outside the fluid domain, but still included by the numerical stencil in at least one fluid node. The procedure of approximating the flow variables in the ghost nodes is as follows. A normal probe is extended from each ghost node to the closest point on the interface, which we call the body intercept point. The same normal probe is extended into the fluid domain to give the position of an image point. We can compute flow variables at the image points by trilinear interpolation of surrounding fluid nodes. As the figure shows, it is also possible to use values from the BC at the body intercept point in the interpolation. The values in the ghost nodes can then be found based on the BC in the body intercept points and the values in the image points.

For Dirichlet conditions, we use linear extrapolation from the image point to the ghost node, meaning that the value at the body intercept point will be the average:

$$\phi_{BI} = \frac{\phi_{GP} + \phi_{IP}}{2} \quad \Longleftrightarrow \quad \phi_{GP} = 2\phi_{BI} - \phi_{IP} \quad . \tag{20}$$

For Neumann conditions the slope will be the prescribed normal gradient:

$$\phi_{GP} = \phi_{IP} - 2|\vec{n}| \cdot \frac{\partial \phi}{\partial \vec{n}} \quad , \tag{21}$$

where $\vec{n}$ is the normal vector from a ghost point to the body intercept point, as seen in Figure 1, and $\frac{\partial \phi}{\partial \vec{n}}$ is the normal gradient in the direction of $\vec{n}$.

4 TEST CASES

4.1 Poiseuille Channel Flow

The 3D Navier-Stokes solver was verified using a Poiseuille channel flow, illustrated in Figure 2. The flow is bounded by two z-normal adiabatic walls, two y-normal artificial boundaries with periodic BCs, and the inlet and outlet planes are normal to the x-axis. For incompressible flow, this type of flow has a steady state 1D analytic solution,

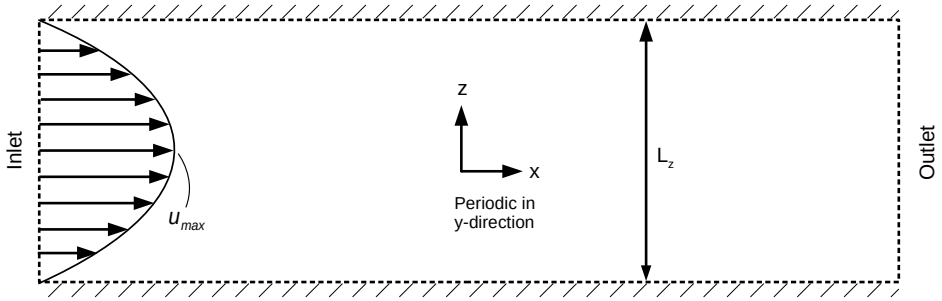

Figure 2: Schematic diagram of the Poiseuille channel flow case.

$$u(z) = \frac{1}{2\mu} \cdot \frac{dp}{dx}(z^2 - L_z z) \quad , \tag{22}$$

which has the extremal value

$$u_{max} = -\frac{L_z^2}{8\mu} \cdot \frac{dp}{dx} \quad , \tag{23}$$

where L_z is the domain size in the z direction, i.e. the channel height.

We used this analytic solution as reference, for low Mach number simulations. Additionally, at the inlet boundary we give this parabola Eq.(22) as BC for the the velocity component u. The other velocity components, v and w, and the temperature perturbation T were set to zero at this boundary, i.e., the temperature at the inlet was set equal to the reference temperature. The pressure perturbation p was linearly extrapolated from the interior. At the outlet the pressure perturbation is kept at zero while mass density and the components of momentum density $\rho u, \rho v, \rho w$ are linearly extrapolated from the interior. For the adiabatic walls, we apply no-slip for the velocities and zero gradients for temperature and pressure. For periodic boundaries, boundary nodes take the values from the boundary adjacent node at the opposite side of the domain.

The initial condition (IC) is stagnation, with all flow variable perturbations at zero, except for the transport properties. To get compatibility with the inlet BC, the parabolic profile for u is ramped up linearly, from zero at $t = 0$ to the analytic solution Eq.(22) at $t \geq 5$.

The Mach number in this case is defined with respect to the maximum velocity u_{max} (23), cf. Figure 2. With the non-dimensionalizing given in Eq.(6) we get simply $Ma = u_{max}$. If we non-dimensionalize Equation (23), we get

$$\frac{dp}{dx} = -\frac{8Ma}{Re_0} \quad , \tag{24}$$

which is a practical expression for comparing the pressure variation to the analytic solution.

4.2 Heat Conduction Between Concentric Cylinders

The 3D IBM to be used with the Navier-Stokes solver has been verified by solving the 3D heat equation,

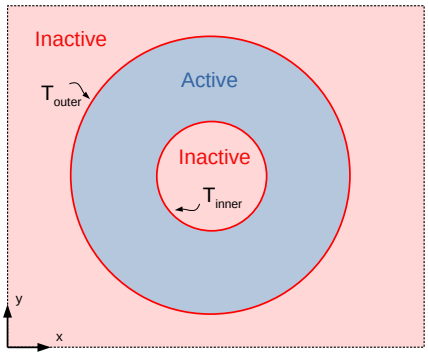

Figure 3: Schematic diagram of the heat conduction test case.

$$\frac{\partial T}{\partial t} = \alpha \nabla^2 T \quad , \tag{25}$$

until steady state, where α is the thermal diffusivity. In this test case the active domain is the annular space between two concentric cylinder faces, as seen in Figure 3. The sketch shows that the computational x-normal and y-normal domain boundaries are not in contact with the active domain. At the z-normal boundaries we apply periodic BCs to model infinitely long cylinders. Dirichlet conditions are prescribed at the cylinder shells, with constant temperatures T_{inner} and T_{outer}.

The steady state analytical solution is given by

$$T = A \cdot ln(r) + B \quad , \tag{26}$$

$$B = \frac{T_{outer} \cdot ln(r_{inner}) - T_{inner} \cdot ln(r_{outer})}{ln(\frac{r_{inner}}{r_{outer}})} \quad , \tag{27}$$

$$A = \frac{T_{inner} - B}{ln(r_{inner})} \quad , \tag{28}$$

where r is the distance from the cylinder centroid, and r_{inner} and r_{outer} are the radii of the cylinder shells.

5 RESULTS

5.1 Channel Flow Case

Results will be presented from three different simulations of the channel flow case. The changing parameter is the Mach number, which was set to 0.01, 0.05 and 0.4. The remaining parameters are listed in Table 1.

Figure 4 shows the velocity profiles at the inlet and outlet, using the different Mach numbers. We can see that the velocity increases downstream. If the flow were incompressible, the velocity would only depend on z, but in this compressible flow the negative pressure gradient dp/dx causes a negative gradient for the mass density. With a lower density, the velocity at the outlet

Table 1: Input parameters for the simulations of the channel flow case. $L_{\{x,y,z\}}$ are the non-dimensional domain sizes. $N_{\{x,y,z\}}$ denote number of grid nodes in each direction.

γ	Pr	Re_0	T_0	L_x	L_y	L_z	N_x	N_y	N_z
1.4	0.72	100	300	5	0.05	1	41	3	41

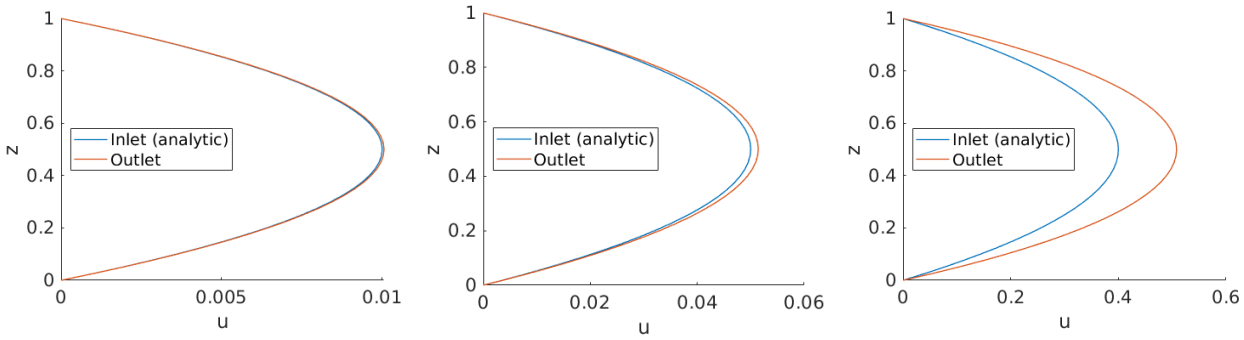

(a) $Ma = 0.01$ (b) $Ma = 0.05$ (c) $Ma = 0.4$

Figure 4: Velocity profiles as functions of z. The blue curves show the values at the inlet $x = 0$, which is the analytic solution. The red curves are the profiles at the outlet $x = L_x$. There is no variation in the y direction, $y = L_y/2$ for all the profiles.

needs to be larger to respect mass conservation. It is seen that the difference between the outlet and inlet velocity profiles increases wit the Mach number, as expected. With the lowest Mach number $Ma = 0.01$ (Figure 4a), the difference in the maximum velocity u_{max} is only 0.6%.

In Figure 5 the pressure variation in the x direction is plotted. With the lower Mach numbers, in figures 5a and 5b, the variation is linear, while Figure 5c displays a small negative curvature. By using the analytic expression Eq.(24) we can find the theoretical pressures at the inlet to be

$$\begin{aligned} \text{p(x=0; Ma=0.01)} &= 0.004 \\ \text{p(x=0; Ma=0.05)} &= 0.02 \\ \text{p(x=0; Ma=0.4)} &= 0.16 \end{aligned} \quad . \tag{29}$$

For $Ma = 0.01$ (Figure 5a), the inlet pressure is only 0.3% higher than the analytic value.

To ensure that the numerical solution is converging, we check that the time derivatives of the conserved variables are going towards zero. In the numerical model this is done by monitoring the 2-norm of the difference between the two latest time levels:

$$\|\phi^{n+1} - \phi^n\|_2 = \sqrt{\Delta x \Delta y \Delta z \sum_{i,j,k} (\phi_{ijk}^{n+1} - \phi_{ijk}^n)^2} \quad . \tag{30}$$

Figure 6 shows the development of these norms throughout the simulation with $Ma = 0.05$. All the plots show the same trend: Oscillations while the flow is developing from the IC, and then log-linear decrease until the simulation is stopped. As an additional measure to test for

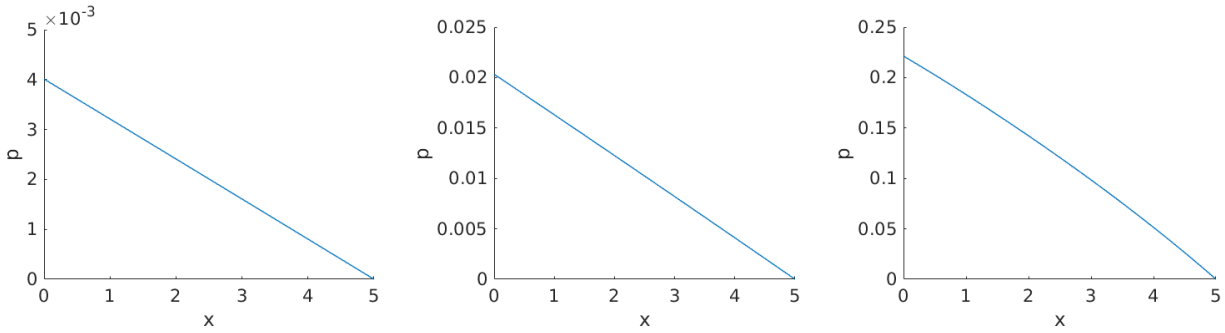

(a) $Ma = 0.01$ (b) $Ma = 0.05$ (c) $Ma = 0.4$

Figure 5: Pressure plotted over x. Values at $y = L_y/2$ and $z = L_z/2$. There is no variation in y, and z variation is negligible.

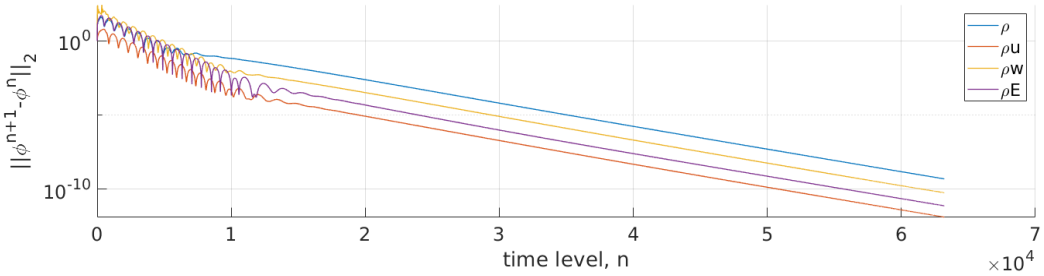

Figure 6: Convergence plot for the channel flow with $Ma = 0.05$. Development of 2-norm of change in conserved variables between time levels. Normalized by the norm of change from the first time step. y momentum omitted, as it is constant zero.

convergence, the difference in mass flux between inlet and outlet was checked. Their relative difference with respect to the inlet mass flux is only about 10^{-8}.

5.2 Heat Conduction Case

The heat conduction test case was simulated six times, with increasing grid resolutions, $N_x = N_y \in \{6, 11, 21, 41, 81, 161\}$, to check the rate of convergence for the method. Figure 7 shows how much the error decreases as the mesh is refined. Apart from the coarsest mesh, with 6x6x3 nodes, the red curve indicates that the order of accuracy is a little above 2.

Figure 8a shows the numerical solution from the simulation with the finest mesh, which looks exactly as expected, considering the analytical solution Eq.(26). The error distribution, shown in Figure 8b, reveals an interesting phenomenon. At the inner boundary we see four regions in the cardinal directions where the error is higher than the rest of the domain. Upon closer inspection we observe that the error is highest around the nodes that lie closest to the immersed boundary.

To investigate if the phenomenon is an artifact of the method or stems from the present solver, the exact same test case was simulated using another solver code. The second code

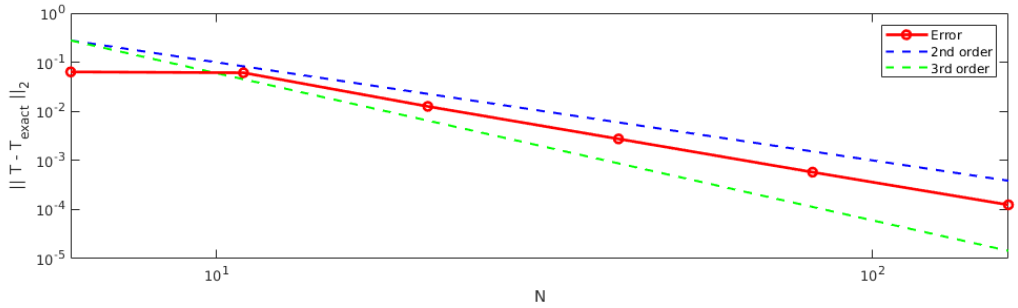

Figure 7: Rate of convergence plot. The error is the 2-norm of the difference between the numerical and the analytical solution. N is the number of grid nodes in the x and y directions.

Table 2: Input parameters for the heat conduction case.

T_{inner}	T_{outer}	r_{inner}	r_{outer}	κ
1	2	0.1999	0.4499	10^{-6}

utilizes the same ghost point IBM, but solves the stationary heat equation directly [13]. The solutions and error distributions are identical, with the largest appearing differences around 10^{-8}, four orders of magnitude lower than the largest error values. The differences are caused by the tolerance of the stopping criterion in the time stepping method to steady state. When the stopping criterion is tightened, the differences get smaller. We therefore conclude that the phenomenon is an artifact of the method.

Other authors have reported similar error hotspots near boundaries, but there has not been much discussion about this in relation to ghost point IBMs. A possible explanation for the artifact could be that when a fluid node is very close to the immersed boundary, the adjacent ghost point will be relatively far away from the boundary. This also increases the distance between the ghost point and image point, which in turn could introduce higher errors. However, this does not explain why the errors are larger at the inner boundary than at the outer. Adjusting the centroid and radii of the cylinders proved to have an effect on which of the error hotspots that show up. Also, if the centroid is not located on a grid node, the symmetries in the error distribution that we see in Figure 8b are naturally lost.

To ensure that the solution is converging, the 2-norm of the changes between time levels were monitored and used as the stopping criterion for this test case. Figure 9 shows the development of the norm through the simulation. It is clear that after an initial development we get log-linear convergence until the simulation is stopped.

6 CONCLUSIONS

The Navier-Stokes solver for compressible flow using 2nd order central difference operators for the spatial discretization and the classical explicit 4th order Runge-Kutta method in time was verified for Poiseuille channel flow. The results agree very well with the incompressible analytical solution, for low Mach numbers.

The 3D IBM was verified for heat conduction between two concentric cylinders. The numer-

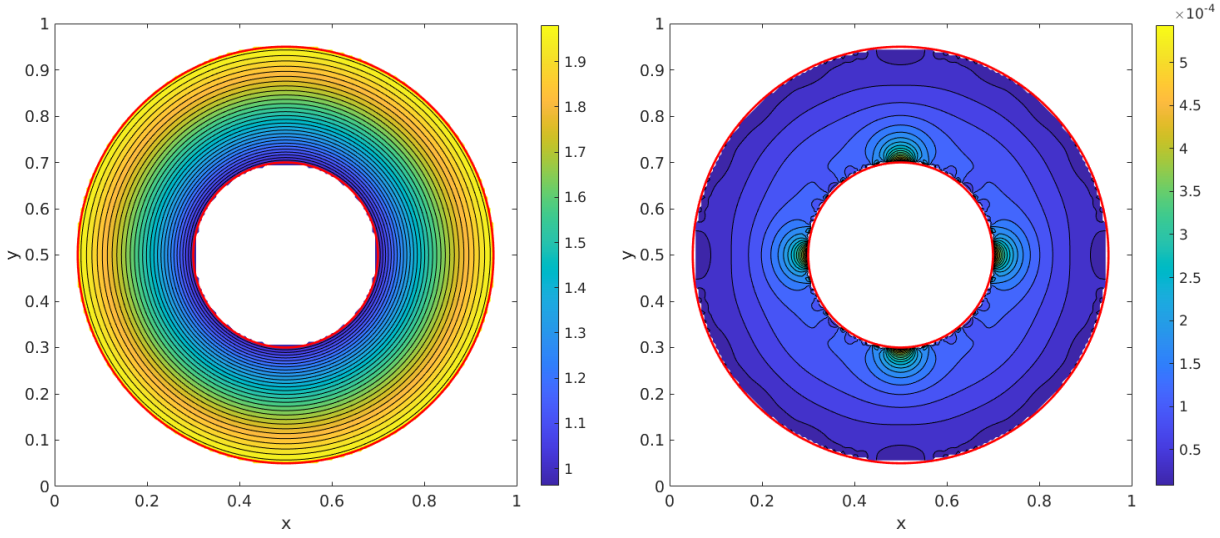

(a) T_{num}, including ghost nodes.

(b) Absolute error, excluding ghost nodes.

Figure 8: Numerical solution and error distribution for the simulation with 161x161x3 nodes.

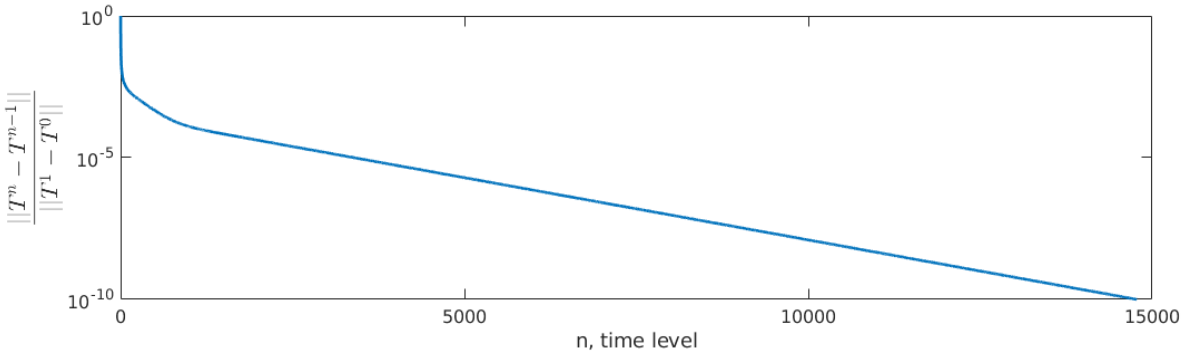

Figure 9: Convergence plot for the heat conduction case with $N = 161$. Development of 2-norm of solution change between time levels.

ical solution was shown to agree very well with the analytical solution. The order of accuracy for the method was indicated to be slightly above second order. Additionally, an interesting artifact of the ghost point IBM was observed in the error distribution, in the form of hotspots close to the inner immersed boundary. A more in-depth analysis is required to find the origin of this phenomenon.

The 3D IBM will be developed for the compressible Navier-Stokes equations and will be coupled to a structure solver to allow FSI simulations of flow in flexible geometries with soft boundaries. The verification results give confidence that the present Navier-Stokes solver and IBM will be a sound basis to tackle complex FSI problems.

ACKNOWLEDGEMENT

The authors acknowledge the funding of the current research by the Research Council of Norway in the research project no. 303218 entitled "Virtual Surgery in the Upper Airways – New Solutions to Obstructive Sleep Apnea Treatment (VirtuOSA)".

REFERENCES

[1] Sacchetti, Lisandro M. and Mangiardi, P. *Obstructive Sleep Apnea : Causes, Treatment and Health Implications*. Nova Science Publishers, (2012)

[2] Ashraf, W. and Jacobson, N. and Popplewell, N. and Moussavi, Z. Fluid–structure interaction modelling of the upper airway with and without obstructive sleep apnea: a review *Med. Biol. Eng. Comput.* (2022) **60**:1827–1849.

[3] Kim, K. B. and McShane, P. G. and McQuilling, M. and Oliver, D. R. and Schauseil, M. Computational airflow analysis before and after maxillomandibular advancement surgery *J. World Fed. Orthod.* (2016) **5(1)**:2–8.

[4] Kim, W. and Choi, H. Immersed boundary methods for fluid-structure interaction: A review. *Int. J. of Heat and Fluid Flow* (2019) **75**:301–309.

[5] Wang, C. and Tang, H. and Zhang, X. Fluid-structure interaction of bio-inspired flexible slender structures: a review of selected topics *Bioinspir. Biomim.* (2022) **17(4)**

[6] Kleinstreuer, C. and Zhang, Z. Airflow and Particle Transport in the Human Respiratory System *Annu. Rev. of Fluid Mech.* (2010) **42**:301–334.

[7] Roy, S. and De, A. and Balaras, E. *Immersed Boundary Method : Development and Applications*. Springer Singapore, 1st ed., (2020).

[8] Choung, H. and Saravanan, V. and Lee, S. Jump-reduced immersed boundary method for compressible flow. *Int. J. Numer. Methods Fluids* (2020) **92(9)**:1135–1161.

[9] Peskin, C. S. Flow patterns around heart valves: A numerical method. *J. Comput. Phys.* (1972) **10**:252–271.

[10] Mittal R. and Iaccarino G. Immersed boundary methods. *Annu. Rev. Fluid Mech.* (2005) **37**:239–261.

[11] Khalili, M. E. and Larsson, M. and Müller, B. Immersed boundary method for viscous compressible flows around moving bodies. *Comput. Fluids* (2018) **170**:77–92.

[12] Sesterhenn, J. and Müller, B. and Thomann, H. On the Cancellation Problem in Calculating Compressible Low Mach Number Flows. *J. Comput. Phys.* (1999) **151**(2):597–615.

[13] Larsson, M. Private communication (2022)